

Extra-cavity manipulating a bright-gray vector soliton

Yan Zhou(周延), Daqian Tang(唐大千), Junxiao Zhan(占军潇), Yang Wang(汪洋), Weijia Zhao(赵炜佳), Meisong Liao(廖梅松), Yongzheng Fang(房永征)
Citation: Chin. Phys. B. 35, 094202 (2026). DOI: 10.1088/1674-1056/ae6d97 |
CSTR: 32038.14.CPB.ae6d97
http://cpb.iphy.ac.cn; http://iopscience.iop.org/cpb

What follows is a list of articles you may be interested in

Multi-mode chirped-Pearcey–Laguerre–Gaussian space–time wave packets synergistically regulated by dispersion and chirp

Yue Du(杜悦), Sai Ma(马赛), Chenchen Li(李晨晨), Haojie Li(李昊杰), Xiaolu Ge(葛筱璐), Chidao Chen(陈迟到), Benyi Wang(王本义), Zhongsheng Man(满忠胜), Wenfei Zhang(张文飞), Liping Zhang(张丽萍)
Chin. Phys. B. 35, 084210 (2026). DOI: 10.1088/1674-1056/ae64cf | CSTR: 32038.14.CPB.ae64cf

Manipulating vector solitons with super-sech pulse shapes

Yan Zhou(周延), Keyun Zhang(张克赟), Chun Luo(罗纯), Xiaoyan Lin(林晓艳), Meisong Liao(廖梅松), Guoying Zhao(赵国营), Yongzheng Fang(房永征)
Chin. Phys. B. 31, 054203 (2022). DOI: 10.1088/1674-1056/ac439f

Polarization manipulation of bright-dark vector bisolitons

Yan Zhou(周延), Xiaoyan Lin(林晓艳), Meisong Liao(廖梅松), Guoying Zhao(赵国营), Yongzheng Fang(房永征)
Chin. Phys. B. 30, 034208 (2021). DOI: 10.1088/1674-1056/abd76d

Pulse shaping of bright-dark vector soliton pair

Yan Zhou(周延), Yuefeng Li(李月锋), Xia Li(李夏), Meisong Liao(廖梅松), Jingshan Hou(侯京山), Yongzheng Fang(房永征)
Chin. Phys. B. 29, 054202 (2020). DOI: 10.1088/1674-1056/ab7b56

Soliton guidance and nonlinear coupling for polarized vector spiraling elliptic Hermite-Gaussian beams in nonlocal nonlinear media

Chunzhi Sun(孙春志), Guo Liang(梁果)
Chin. Phys. B. 28, 074206 (2019). DOI: 10.1088/1674-1056/28/7/074206

SPECIAL TOPIC — Nonlinear localized waves: Theory, methods and applications

Extra-cavity manipulating a bright-gray vector soliton

Yan Zhou(周延)[1,†], Daqian Tang(唐大千)[1], Junxiao Zhan(占军潇)[1], Yang Wang(汪洋)[1], Weijia Zhao(赵炜佳)[1], Meisong Liao(廖梅松)[2], and Yongzheng Fang(房永征)[3,‡]

[1] *School of Sciences, Shanghai Institute of Technology, Shanghai* 201418, *China*

[2] *Advanced Laser and Optoelectronic Functional Materials Department, Special Glasses and Fibers Research Center, Shanghai Institute of Optics and Fine Mechanics, Chinese Academy of Sciences, Shanghai* 201800, *China*

[3] *Faculty of Materials Technology, Shanghai Institute of Technology, Shanghai* 201418, *China*

(Received 6 February 2026; revised manuscript received 12 May 2026; accepted manuscript online 14 May 2026)

Both intra-cavity and extra-cavity manipulation of optical solitons are efficient methods for investigating the dynamic properties of solitons in nonlinear optical systems. In this article, we mainly simulate the extra-cavity manipulation of a bright-gray vector soliton at a wavelength of 1064 nm, considering that the bright soliton component and gray soliton component have the same or slightly different central wavelengths. Five kinds of soliton parameters (including central wavelengths) are varied based on our proposed extra-cavity manipulation physical system. Both single-parameter variation and dual-parameter variation methods are adopted in the simulation. The manipulated bright-gray vector soliton's pulse shapes and optical spectra in orthogonal polarizations will exhibit unique characteristics when different parameters are varied. For instance, slightly different central wavelengths can induce obvious temporal oscillations of orthogonally polarized pulse shapes at the output terminal. Our simulations effectively explore the manipulation of different types of optical solitons in extra-cavity manipulation systems, providing useful reference for studying the nonlinear dynamics of various types of optical solitons in extra-cavity manipulation systems.

Keywords: vector soliton, manipulation, polarization

PACS: 42.65.Tg, 42.81.Gs, 42.55.–f

DOI: 10.1088/1674-1056/ae6d97 **CSTR:** 32038.14.CPB.ae6d97

1. Introduction

In the field of nonlinear fiber optics, the study of optical solitons has always been a hotspot over the past decades.[1–7] Optical solitons can propagate in optical fibers and maintain their pulse shapes and velocities over long transmission distances, making them applicable to long-distance and high-speed optical fiber communications. Optical solitons can exist in the normal dispersion regime ($\lambda < 1.3$ μm), zero-dispersion position ($\lambda = 1.3$ μm), or anomalous dispersion regime ($\lambda > 1.3$ μm), under the balance of different parameters, such as self-phase modulation, group-velocity dispersion, optical spectral filtering, linear birefringence, gain, loss and higher-order dispersions. Generally, optical solitons are usually studied in mode-locked fiber laser cavities,[8–18] thanks to their compact structures, high heat dissipation efficiency, ease of changing different parameters, ease of maintenance and strong anti-electromagnetic interference capability. As a kind of highly efficient intra-cavity manipulated optical fiber system, mode-locked fiber lasers can generate optical soliton pulses with different pulse widths (from ns to fs pulses), repetition rates (from kHz to THz), single pulse energies (at nJ level for optical fiber laser oscillators), polarizations (linearly polarized or elliptically polarized), central wavelengths (from visible band to mid-infrared band), pulse shapes (sech shape, rectangle shape, sech^2 shape, parabolic shape, Gaussian shape) and so on.

Optical solitons in nonlinear optical fiber systems can be classified into two categories: one is scalar solitons and the other is vector solitons. Ideal scalar solitons exist in all polarization-maintained mode-locked fiber lasers.[19] And scalar approximation is often adopted in single-mode or multimode fiber lasers, through the compensation of linear birefringence by adjusting intra-cavity polarization controller. By comparison, vector solitons exist in birefringent environments, which are produced by polarization elements, such as polarization-maintained fibers and linear polarizers.[20–26] Among these vector solitons, bright-gray vector soliton has a bright soliton in one polarization direction, and a gray soliton in the orthogonal polarization direction. Bright soliton and gray soliton are coupled together through nonlinear interaction, and can co-propagate over a long distance without distortion in the time or frequency domain. The theoretical simulations of scalar and vector solitons in fiber lasers can be numerically or analytically solved with corresponding master equations, including nonlinear Schrödinger equa-

†Corresponding author. E-mail: yzhou@sit.edu.cn

‡Corresponding author. E-mail: fyz1003@sina.com

© 2026 Chinese Physical Society and IOP Publishing Ltd. All rights, including for text and data mining, AI training, and similar technologies, are reserved.

tion (NSE),[27] coupled NSEs,[28] Ginzburg–Landau equation (GLE),[29] coupled GLEs.[30] The theoretical and experimental research on optical solitons in optical fiber manipulation systems efficiently promotes developments in the fields of optical communications and optical information processing.

Except for the intra-cavity manipulated mode-locked (including active and passive) fiber lasers, extra-cavity manipulation of optical solitons is attracting great interest from researchers, due to its larger parameter tuning range and flexible parameter adjustment methods. To date, some studies have been conducted on extra-cavity manipulation of different types of scalar solitons and vector solitons, in normal or anomalous dispersion regimes.[31,32] However, there are few reports on the extra-cavity manipulation of bright-gray vector solitons. In this work, we propose an extra-cavity soliton manipulation system and theoretically simulate the extra-cavity manipulation of a bright-gray vector soliton at the 1064 nm wavelength band, which is applicable to ytterbium-doped vector soliton fiber lasers. The simulations systematically analyze the influences of different soliton parameters on the time- and frequency-domain characteristics of the input bright-gray vector soliton. The simulation results reveal the nonlinear dynamics of a bright-gray vector soliton when different soliton parameters are varied.

2. Description of theoretical model

Figure 1 gives our proposed extra-cavity optical soliton manipulation system on which our simulations are based. Obviously, this manipulation system has a spatial optical structure. The bright-gray vector soliton is generated from a vector soliton mode-locked ytterbium-doped fiber laser source. Firstly, the orthogonal components of the input bright-gray vector soliton are separated by a polarization beam splitter (PBS1). Then, both horizontal and vertical electric fields are manipulated by the two variable optical attenuators (VOA1 and VOA2). The time delay between the orthogonal electric fields is varied by tuning the two optical delay lines (ODL1 and ODL2). After that, the manipulated horizontal and vertical electric fields are combined with the help of PBS2, and the polarization of the combined electric fields is further manipulated by rotating $\lambda/2$ and $\lambda/4$ wave plates. Finally, the orthogonal electric fields of the manipulated bright-gray vector soliton are split by PBS3. M1 and M2 are two reflective mirrors. PBS1 can be rotated to efficiently separate the orthogonally polarized bright soliton and gray soliton. PBS3 can also be rotated to change the projection angle of the orthogonal electric fields. This manipulation system is applicable to manipulating bright-gray vector solitons at other wavelength bands, but the relevant manipulation elements should be replaced to meet the requirements of the working wavelengths.

The orthogonal electric fields that are incident on PBS3 are

$$u_1(t) = u_1\left[1 - b^2\,\mathrm{sech}^2\left(\frac{t-\Delta T/2}{T_0}\right)\right]\mathrm{e}^{\mathrm{i}\frac{2\pi ct}{\lambda_1}}, \tag{1}$$

$$u_2(t) = u_2\,\mathrm{sech}\left(\frac{t+\Delta T/2}{T_0}\right)\mathrm{e}^{\mathrm{i}\left(\frac{2\pi ct}{\lambda_2}+\Delta\varphi\right)}. \tag{2}$$

Here, $u_1(t)$ and $u_2(t)$ denote the time-varying electric fields in orthogonal directions, while u_1 and u_2 represent the amplitudes in the corresponding polarization directions. b is a dip intensity depth parameter of the gray soliton component ($0 < b < 1$). t denotes the time variable. ΔT denotes the time delay between the bright soliton and gray soliton. T_0 is the pulse width parameter. c (3×10^8 m/s) is the light propagation speed. λ_1 and λ_2 denote the central wavelengths of the bright soliton and gray soliton, which can be the same or different. $\Delta\varphi$ is the total phase difference between the bright component and gray component, and it can be varied by rotating the wave plates. i represents the imaginary unit.

The orthogonal electric fields that are transmitted or reflected by PBS3 are

$$\begin{bmatrix} u_x(t) \\ u_y(t) \end{bmatrix} = \begin{bmatrix} \cos\theta & \sin\theta \\ \sin\theta & -\cos\theta \end{bmatrix} \begin{bmatrix} u_1(t) \\ u_2(t) \end{bmatrix}. \tag{3}$$

θ represents the projection angle, and $u_x(t)$ and $u_y(t)$ are the projected electric fields. Then, the manipulated pulse shapes and optical spectra at the output terminal are defined as

$$I(t) = |u_m(t)|^2, \quad m = x \text{ or } y, \tag{4}$$

$$I(\omega) = |u_m(\omega)|^2 = \left|\int_{-\infty}^{\infty} u_m(t)\,\mathrm{e}^{-\mathrm{i}\omega t}\,\mathrm{d}t\right|^2, \quad m = x \text{ or } y. \tag{5}$$

$I(t)$ is the pulse intensity, and $I(\omega)$ is the optical spectral intensity. m represents the polarization direction.

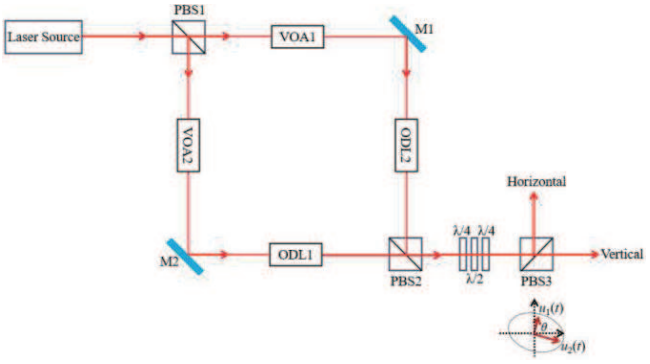


Fig. 1. Our proposed optical soliton manipulation system schematic.

3. Simulation

3.1. Single-parameter variation

In the first part of the single-parameter variation, we assume $\lambda_1 = \lambda_2 = 1064$ nm, meaning that the bright soliton has the same central wavelength as the gray soliton component. In the second part of our simulation, slightly different central

wavelengths are assumed ($\lambda_1 = 1063$ nm, $\lambda_2 = 1065$ nm) for the input bright-gray vector soliton pair. Besides, we assume $T = 5$ ps and $b = 0.9$.

Figure 2 gives the simulated pulses and optical spectra in horizontal and vertical polarizations, when $u_2/u_1 = 1/1.3$, $1/1.2$, $1/1$, $1.2/1$, and $1.3/1$. Meanwhile, $\theta = 0°$, $\Delta T = 0$ ps, $\Delta\varphi = 0$. As demonstrated in Figs. 2(a)–2(e), as u_2/u_1 increases, the bright soliton's amplitude starts to increase when $u_2/u_1 = 1/1$. By comparison, the gray soliton's dip intensity depth decreases (accompanied by decreased intensity of the continuous-wave background) as u_2/u_1 increases from 1/1.3 to 1/1, and the dip intensity will approach zero during this process. For the optical spectra in Figs. 2(f)–2(j), the horizontally and vertically polarized optical spectral peak intensities have the same variation trends as their corresponding pulse shapes when u_2/u_1 increases. The optical spectra in orthogonal polarizations will become more similar to each other as u_2/u_1 increases. When $u_2/u_1 = 1/1$, the temporal peak intensity of the bright soliton is almost the same as the dip intensity depth of the gray soliton, but their corresponding optical spectra have an obvious difference in peak intensity.

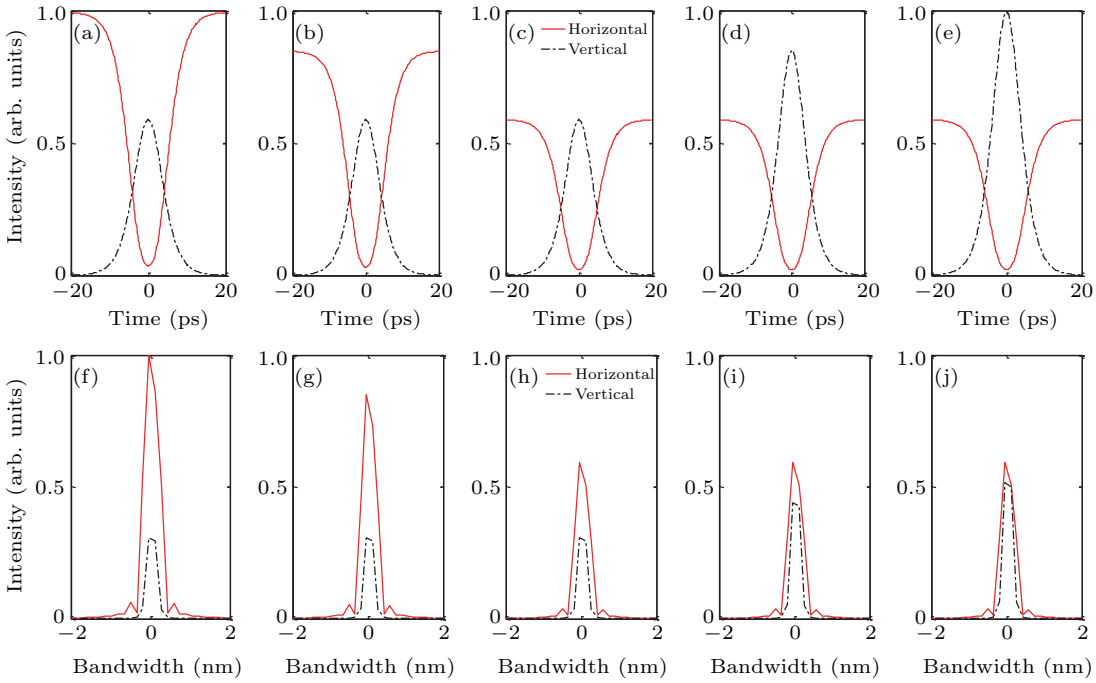


Fig. 2. Simulated pulses and optical spectra in orthogonal polarizations as u_2/u_1 changes ($\lambda_1 = \lambda_2$).

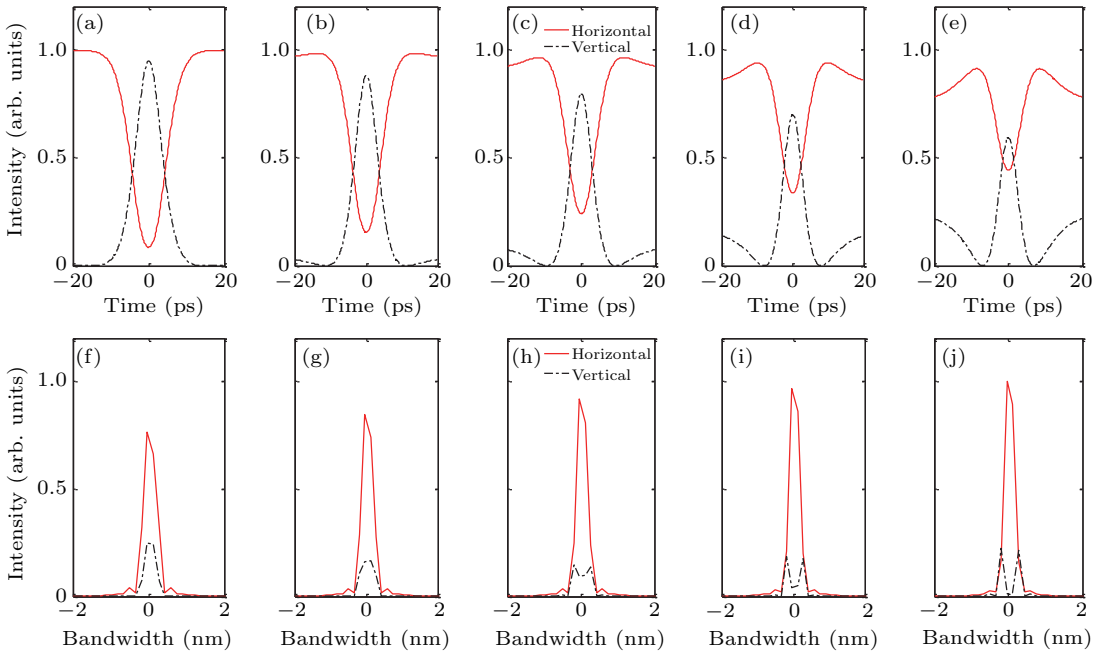


Fig. 3. Simulated pulses and optical spectra in orthogonal polarizations as θ changes ($\lambda_1 = \lambda_2$).

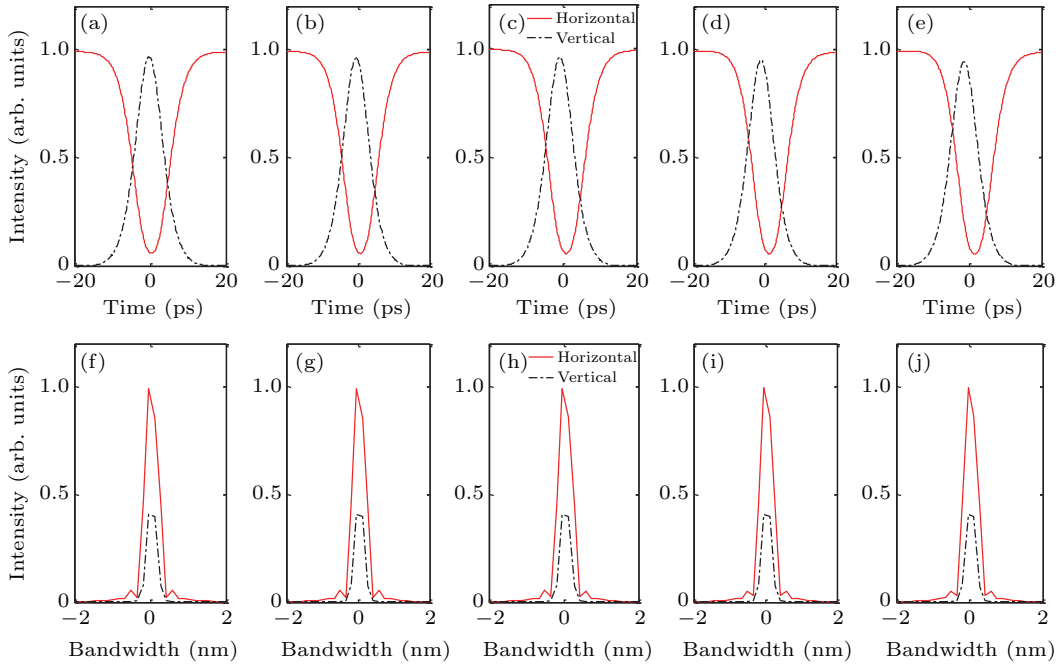


Fig. 4. Simulated pulses and optical spectra in orthogonal polarizations as ΔT changes ($\lambda_1 = \lambda_2$).

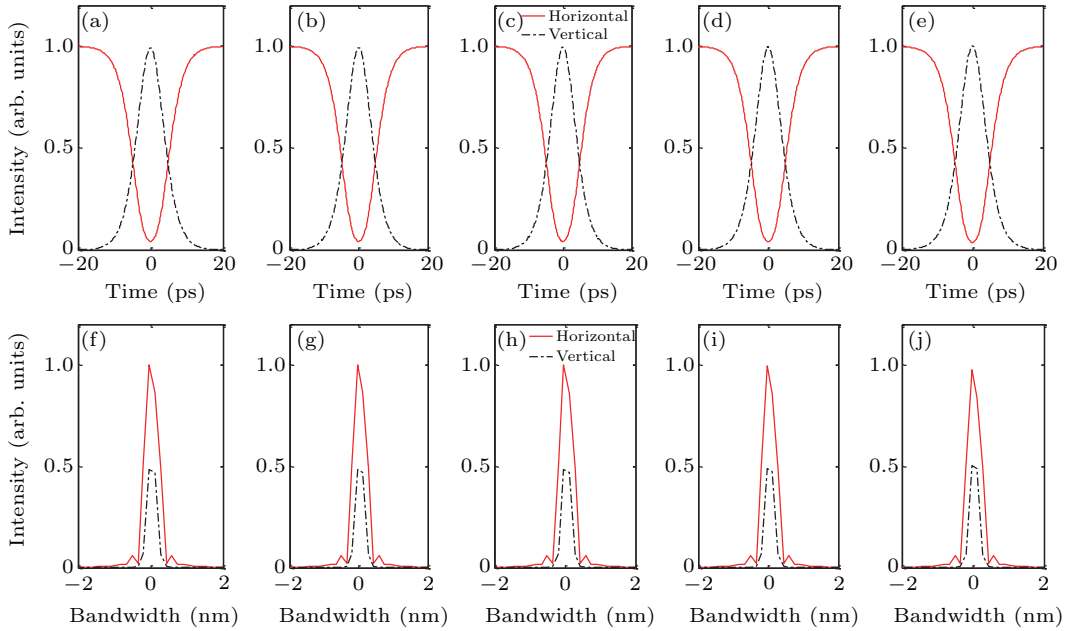


Fig. 5. Simulated pulses and optical spectra in orthogonal polarizations as $\Delta\varphi$ changes ($\lambda_1 = \lambda_2$).

Figure 3 gives the simulated temporal and spectral results in horizontal and vertical polarizations when $\theta = 6°$, $12°$, $18°$, $24°$, and $30°$. Meanwhile, $u_2/u_1 = 1/1$, $\Delta T = 0$ ps, $\Delta\varphi = 0$. In Figs. 3(a)–3(e), the bright soliton's peak intensity decreases and the gray soliton's dip intensity increases as θ increases. Besides, the two wings of the bright soliton have an upward trend, while the two wings of the gray soliton have a downward trend when the projection angle increases. In Figs. 3(f)–3(j), the peak intensity of the horizontal component increases as θ increases. During this process, optical spectrum splitting occurs for the vertical component. There are two obvious peaks in the vertical optical spectrum when $\theta = 24°$ or $30°$. From the results presented in Fig. 3, the following conclusion can be drawn: the orthogonal polarization components of the bright-gray vector soliton are sensitive to variations in the projection angle in both the time and frequency domains.

Figure 4 gives the simulated pulses and optical spectra in horizontal and vertical polarizations when $\Delta T = 0.6$ ps, 1.2 ps, 1.8 ps, 2.4 ps, and 3 ps. Meanwhile, $u_2/u_1 = 1/1$, $\theta = 3°$, $\Delta\varphi = 0$. In Figs. 4(a)–4(e), the pulse shapes of the vertical bright soliton and horizontal gray soliton are invariant as ΔT varies. The time delay between the bright soliton and gray soliton increases with increasing ΔT. For the optical spectral results given by Figs. 4(f)–4(j), the gray soliton's optical spec-

trum always has a higher peak intensity than the bright soliton's. Moreover, there are no obvious changes in the peak intensities and 3 dB bandwidths of the orthogonal components, meaning that the orthogonal optical spectra of the bright-gray vector soliton are robust to changes in ΔT.

Figure 5 gives the simulated pulses and optical spectra in horizontal and vertical polarizations when $\Delta\varphi = \pi/10$, $\pi/8$, $\pi/6$, $\pi/4$, and $\pi/2$. Meanwhile, $u_2/u_1 = 1/1$, $\theta = 1°$, $\Delta T = 0$ ps. From the results in Fig. 5, we can see that as $\Delta\varphi$ increases, both the pulse shapes and optical spectra are almost invariant in both horizontal and vertical polarizations. This means that the bright-gray vector soliton is robust under variations in the orthogonal phase difference. It should be mentioned that when $\Delta\varphi$ further increases from $\pi/2$ to π, the optical spectral peak intensity of the horizontal mode decreases, while that of the vertical mode increases. For the corresponding soliton pulses, the continuous-wave background intensity of the horizontal gray soliton has a slight reduction, while the peak intensity of the vertical bright soliton has a slight enhancement.

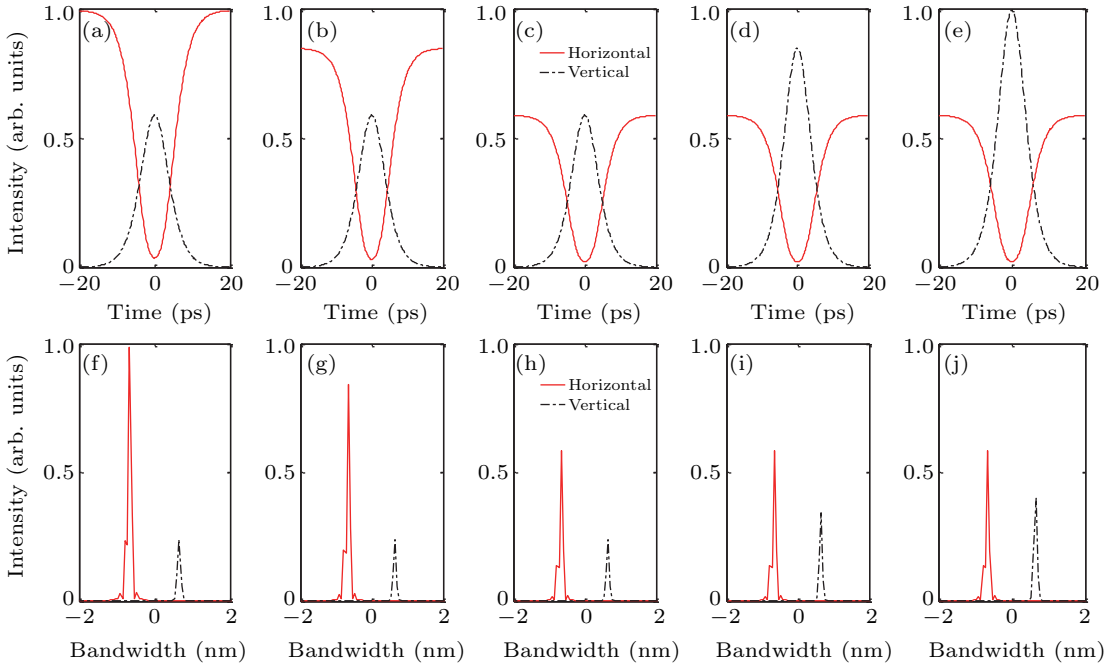


Fig. 6. Simulated pulses and optical spectra in orthogonal polarizations as u_2/u_1 changes ($\lambda_1 \neq \lambda_2$).

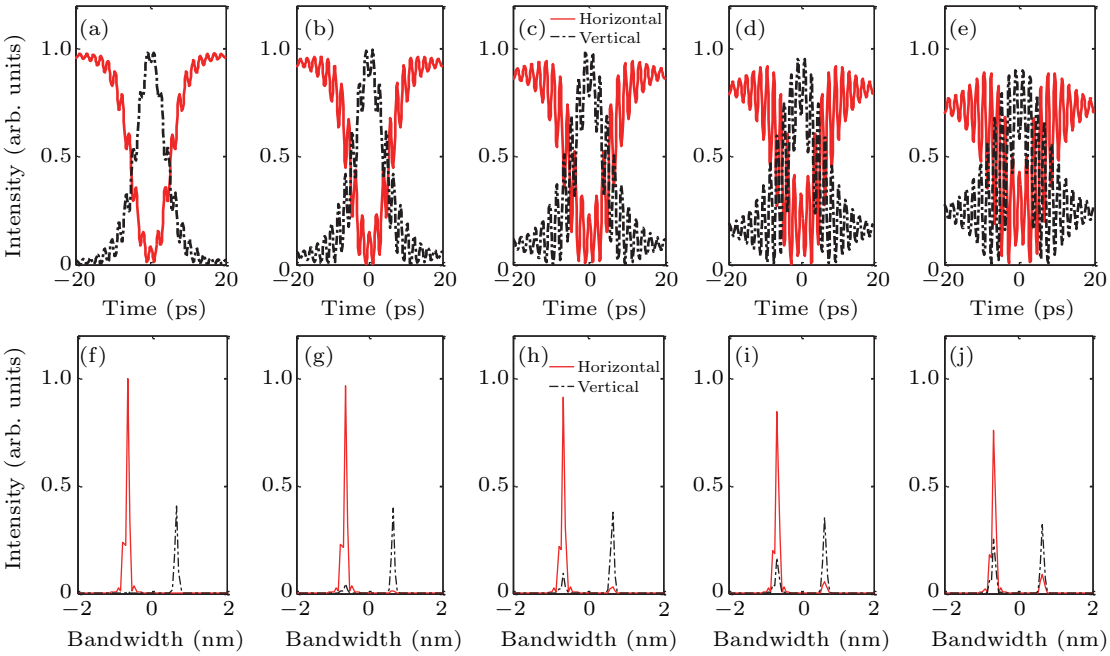


Fig. 7. Simulated pulses and optical spectra in orthogonal polarizations as θ changes ($\lambda_1 \neq \lambda_2$).

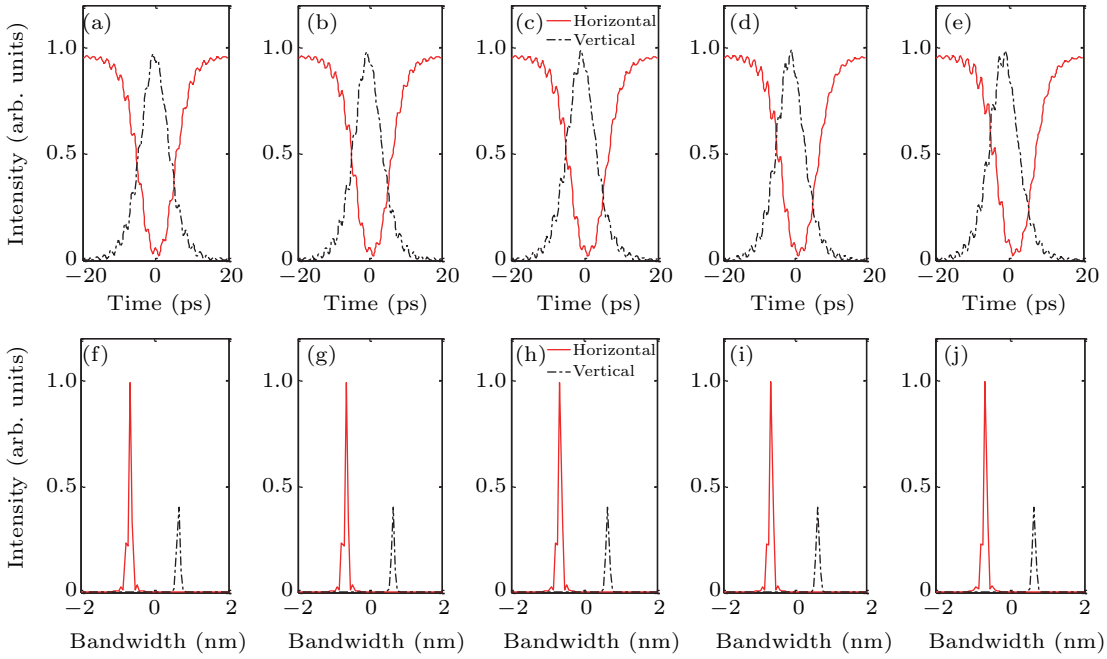


Fig. 8. Simulated pulses and optical spectra in orthogonal polarizations as ΔT changes ($\lambda_1 \neq \lambda_2$).

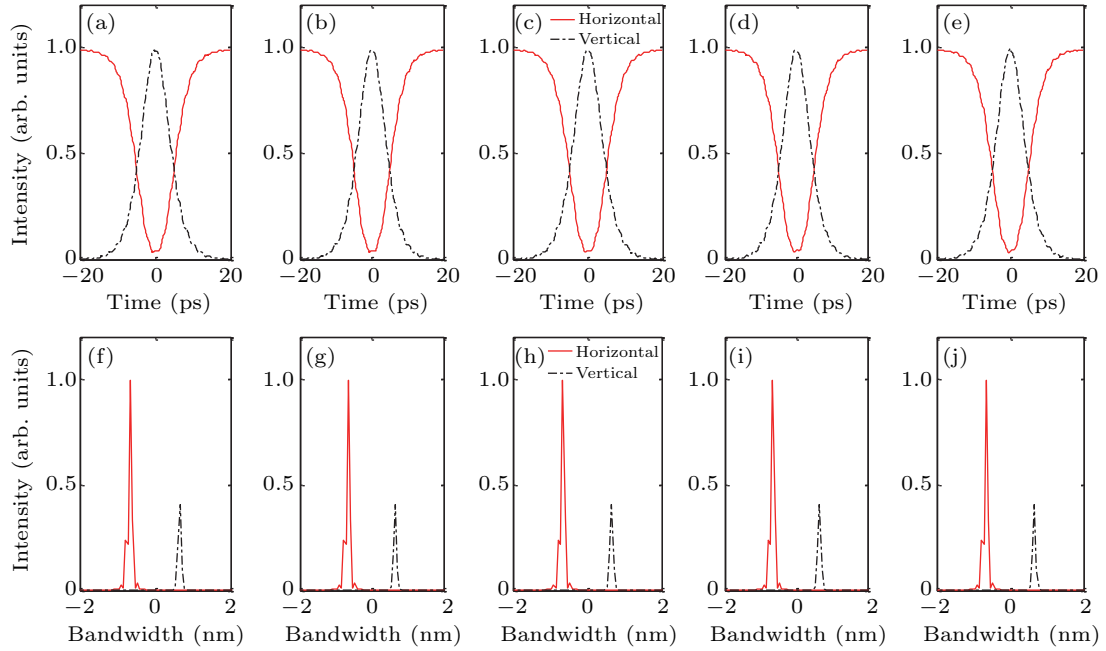


Fig. 9. Simulated pulses and optical spectra in orthogonal polarizations as $\Delta\varphi$ changes ($\lambda_1 \neq \lambda_2$).

Figure 6 gives the simulated pulses and optical spectra in horizontal and vertical polarizations, when $u_2/u_1 = 1/1.3$, 1/1.2, 1/1, 1.2/1 and 1.3/1. Meanwhile, $\lambda_1 = 1063$ nm, $\lambda_2 = 1065$ nm, $\theta = 0°$, $\Delta T = 0$ ps, $\Delta\varphi = 0$. The pulse shapes in Figs. 6(a)–6(e) are the same as those in Figs. 2(a)–2(e), although the orthogonal central wavelengths are different. However, the optical spectra in Figs. 6(f)–6(j) are obviously different from those in Figs. 2(f)–2(j), due to the initial condition of $\lambda_1 \neq \lambda_2$. In Figs. 6(f)–6(j), the horizontal optical spectral peak intensity decreases when u_2/u_1 increases from 1/1.3 to 1/1, and the vertical optical spectral peak intensity starts to increase when $u_2/u_1 = 1/1$. The peak wavelength difference between the orthogonal bright soliton and gray soliton is ~ 4 nm, which is larger than the initial 2 nm.

Figure 7 gives the simulated pulses (a)–(e) and optical spectra (f)–(j) in horizontal and vertical polarizations, when $\theta = 6°$, 12°, 18°, 24° and 30°. Meanwhile, $\lambda_1 = 1063$ nm, $\lambda_2 = 1065$ nm, $u_2/u_1 = 1/1$, $\Delta T = 0$ ps and $\Delta\varphi = 0$. It is obvious that both orthogonal pulse shapes and optical spectra in Fig. 7 are different from those in Fig. 3. In Figs. 7(a)–7(e), temporal pulse oscillations occur for both the bright soliton and gray soliton, and the oscillation behavior becomes more obvious as θ increases from 6° to 30°. In Figs. 7(f)–7(j), the peak intensity of the horizontal component at the 1062 nm

position decreases with increasing θ, which induces the appearance and increased peak intensity of another peak at the 1066 nm position in the same polarization direction. During this process, the peak intensity of the vertical component at the 1066 nm position decreases, and the newly appeared optical spectral peak at the 1062 nm position in the vertical direction increases with increasing θ. These simulation results indicate that the change in θ (when $\lambda_1 \neq \lambda_2$) will induce soliton energy flow at two different wavelengths.

Figure 8 gives the simulated pulses and optical spectra in horizontal and vertical polarizations, when $\Delta T = 0.6$ ps, 1.2 ps, 1.8 ps, 2.4 ps and 3 ps. Meanwhile, $\lambda_1 = 1063$ nm, $\lambda_2 = 1065$ nm, $u_2/u_1 = 1/1$, $\theta = 3°$, $\Delta\varphi = 0$. In Figs. 8(a)–8(e), the time delay between the bright soliton and gray soliton increases with increasing ΔT, and is always accompanied by slight temporal pulse oscillations in the orthogonal soliton pulses. The temporal oscillations are less obvious than those in the results in Figs. 7(a)–7(e), meaning that the projection angle is the main factor that influences the temporal oscillations of the orthogonal components when $\lambda_1 \neq \lambda_2$. In Figs. 8(f)–8(j), the horizontal component's peak intensity is always higher than the vertical component's peak intensity, and both orthogonal optical spectra show no obvious changes when ΔT changes.

Figure 9 gives the simulated pulses (a)–(e) and optical spectra (f)–(j) in horizontal and vertical polarizations, when $\Delta\varphi = \pi/10$, $\pi/8$, $\pi/6$, $\pi/4$ and $\pi/2$. Meanwhile, $\lambda_1 = 1063$ nm, $\lambda_2 = 1065$ nm, $u_2/u_1 = 1/1$, $\theta = 1°$, $\Delta T = 0$ ps. The bright soliton and gray soliton show no obvious changes in either the time or frequency domains as $\Delta\varphi$ varies. If $\Delta\varphi$ further increases from $\pi/2$ to π, the bright-gray vector soliton is still robust to variations in $\Delta\varphi$, which is different from the case of $\lambda_1 = \lambda_2$. Therefore, we can conclude that the bright-gray vector soliton with different central wavelengths has improved robustness compared with the bright-gray vector soliton with the same central wavelength under variations in phase difference. This property makes the bright-gray vector soliton with different central wavelengths more applicable to polarization-multiplexed long-distance optical information processing, because of the accumulated phase difference in single-mode fibers over a length of tens of kilometers.

3.2. Dual-parameter variation

Similar to Subsection 3.1, in the first part of the dual-parameter variation, we assume $\lambda_1 = \lambda_2 = 1064$ nm. In the second part, slightly different central wavelengths are assumed ($\lambda_1 = 1063$ nm, $\lambda_2 = 1065$ nm) for the orthogonal components of the input bright-gray vector soliton. Besides, we assume $T = 5$ ps, $b = 0.9$.

Figure 10 gives the simulated pulses and optical spectra in horizontal and vertical polarizations ($\lambda_1 = \lambda_2$), when $u_2/u_1 = 1/1.3$, $1/1.2$, $1/1$, $1.2/1$ and $1.3/1$. Meanwhile, $\theta = 5°$, $10°$, $15°$, $20°$ and $25°$. $\Delta T = 0$ ps, $\Delta\varphi = 0$. In Figs. 10(a)–10(e), the peak intensity of the vertical pulse will decrease and then increase as u_2/u_1 and θ increase. During this evolution process, the continuous-wave background intensity of the horizontal pulse has the same variation tendency. For the orthogonal optical spectra in Figs. 10(f)–10(j), the peak intensities have the same variation trends as the corresponding pulse shapes. Obvious optical spectrum splitting

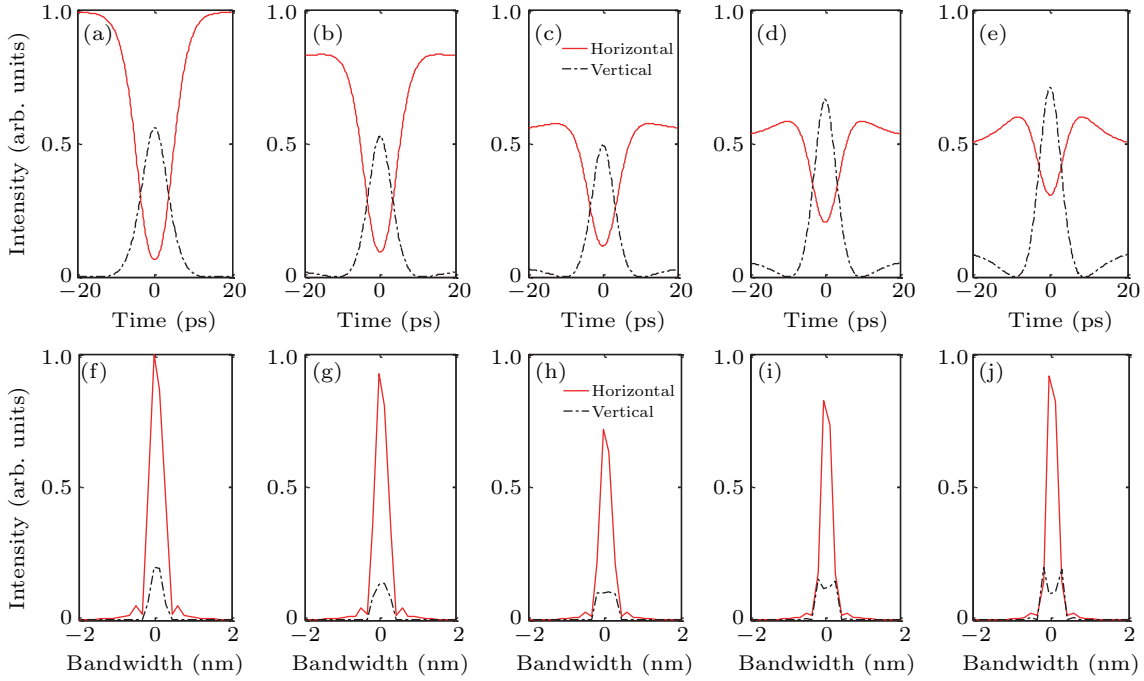


Fig. 10. Simulated pulses and optical spectra in orthogonal polarizations as u_2/u_1 and θ change ($\lambda_1 = \lambda_2$).

occurs for the vertical mode when $u_2/u_1 = 1.3/1$ and $\theta = 25°$. This means that the increase of u_2/u_1 increases the threshold of θ required for optical spectral splitting in the vertical polarization direction, compared with the results in Figs. 3(f)–3(j).

Figure 11 gives the simulated pulses and optical spectra in horizontal and vertical polarizations ($\lambda_1 = \lambda_2$), when $\Delta T = 0.6$ ps, 1.2 ps, 1.8 ps, 2.4 ps and 3 ps. Meanwhile, $\Delta\varphi = \pi/10$, $\pi/9$, $\pi/8$, $\pi/7$ and $\pi/6$. $u_2/u_1 = 1/1$, $\theta = 3°$. In Figs. 11(a)–11(e), we can see that as ΔT and $\Delta\varphi$ increase, the time delay between the horizontal gray soliton and vertical bright soliton also increases, without obvious changes in the pulse shapes. Similarly, the orthogonal optical spectra in Figs. 11(f)–11(j) can maintain their states under simultaneous variations of ΔT and $\Delta\varphi$.

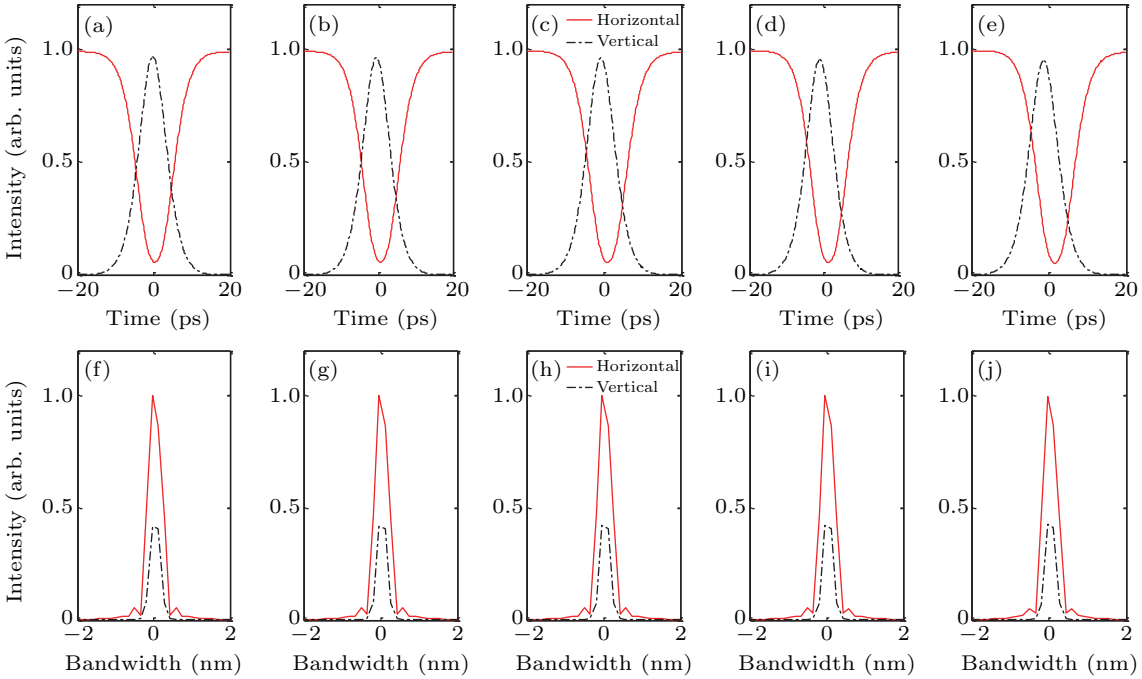


Fig. 11. Simulated pulses and optical spectra in orthogonal polarizations as ΔT and $\Delta\varphi$ change ($\lambda_1 = \lambda_2$).

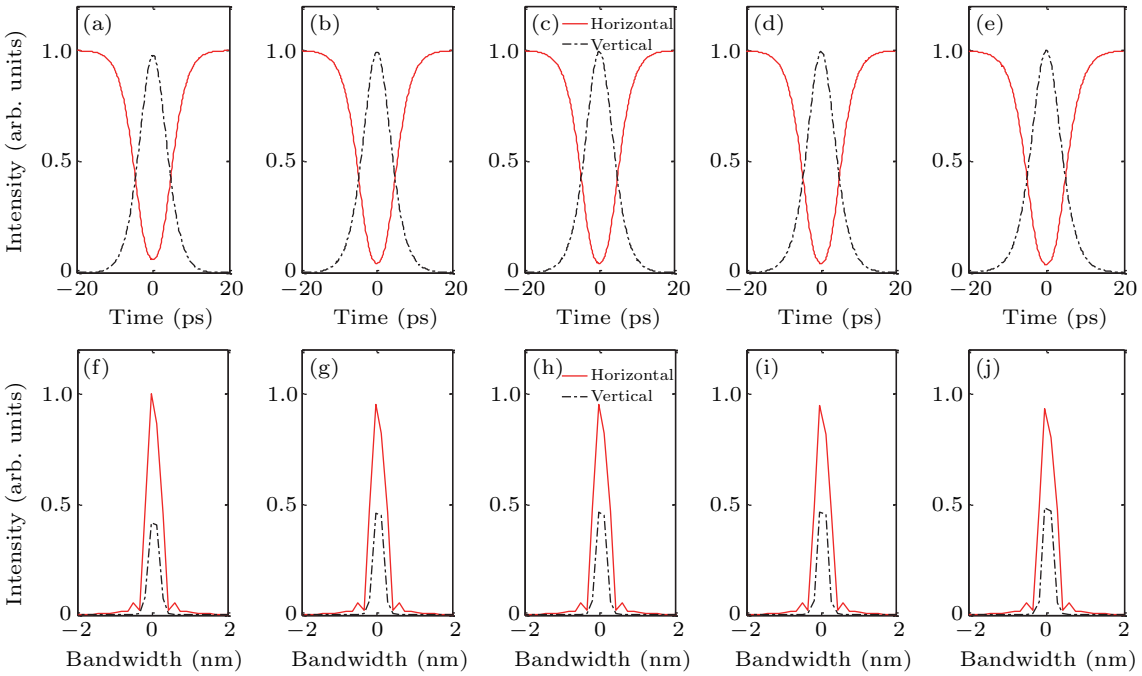


Fig. 12. Simulated pulses and optical spectra in orthogonal polarizations as θ and $\Delta\varphi$ change ($\lambda_1 = \lambda_2$).

Figure 12 gives the simulated pulses and optical spectra in horizontal and vertical polarizations ($\lambda_1 = \lambda_2$), when $\theta = 3°$, 6°, 9°, 12°, and 15°. Meanwhile, $\Delta\varphi = \pi/10$, $\pi/9$, $\pi/8$, $\pi/7$, and $\pi/6$. $u_2/u_1 = 1/1$, $\Delta T = 0$ ps. We can see that both soliton pulses and their optical spectra in orthogonal directions are invariant under simultaneous changes of θ and $\Delta\varphi$. So we can

conclude that the increased $\Delta\varphi$ can efficiently compensate for the variations in pulse shapes and optical spectra induced by θ.

Figure 13 shows the simulated pulses and optical spectra in horizontal and vertical polarizations ($\lambda_1 \neq \lambda_2$), when $u_2/u_1 = 1/1.3$, 1/1.2, 1/1, 1.2/1 and 1.3/1. Meanwhile, $\theta = 5°$, 10°, 15°, 20° and 25°. $\Delta T = 0$ ps, $\Delta\varphi = 0$. Temporal oscillations always exist for orthogonal pulses in Figs. 13(a)–13(e). The horizontal pulse's continuous-wave background intensity will decrease and then slightly increase when both u_2/u_1 and θ increase. While the vertical pulse's peak intensity has slight variation at the beginning, it starts to increase when $u_2/u_1 = 1/1$ and $\theta = 15°$. In Figs. 13(f)–13(j), the peak intensity of the shorter-wavelength component decreases with increasing u_2/u_1 and θ, and another longer-wavelength peak occurs when $u_2/u_1 = 1/1$ and $\theta = 15°$, in the horizontal polarization direction. By comparison, the vertical mode converts from a single-wavelength state to a dual-wavelength state when $u_2/u_1 = 1/1$ and $\theta = 15°$. Then, the peak intensities of both the shorter- and longer-wavelength components increase with increasing u_2/u_1 and θ, meaning that energy flow occurs between the orthogonal modes.

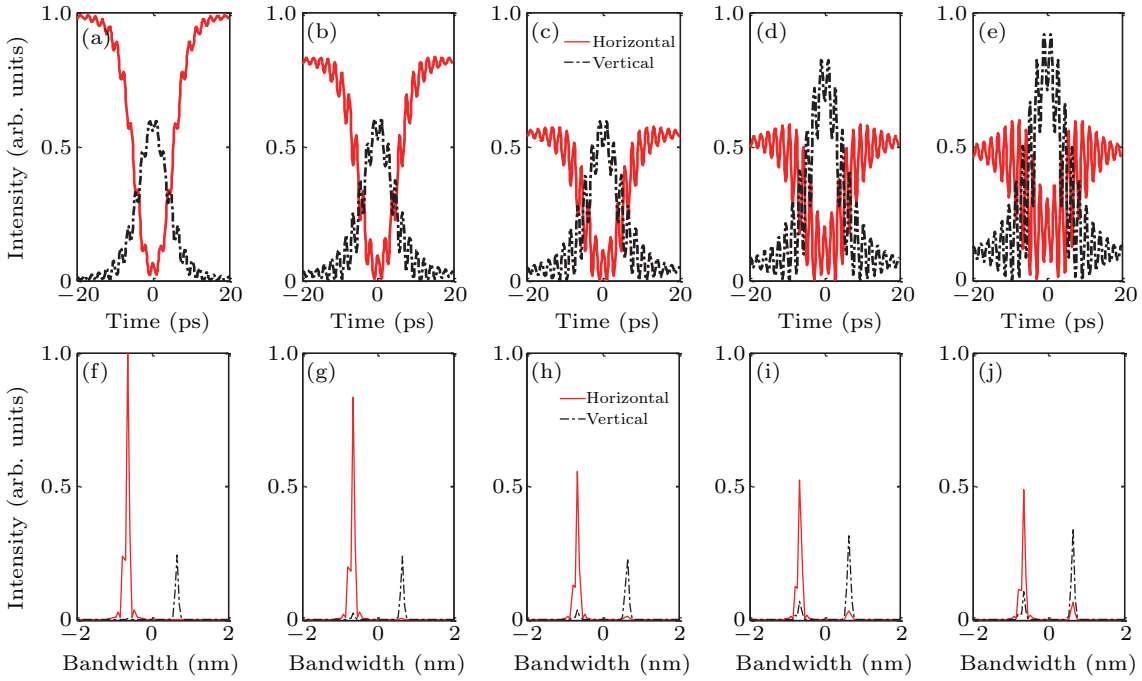


Fig. 13. Simulated pulses and optical spectra in orthogonal polarizations as u_2/u_1 and θ change ($\lambda_1 \neq \lambda_2$).

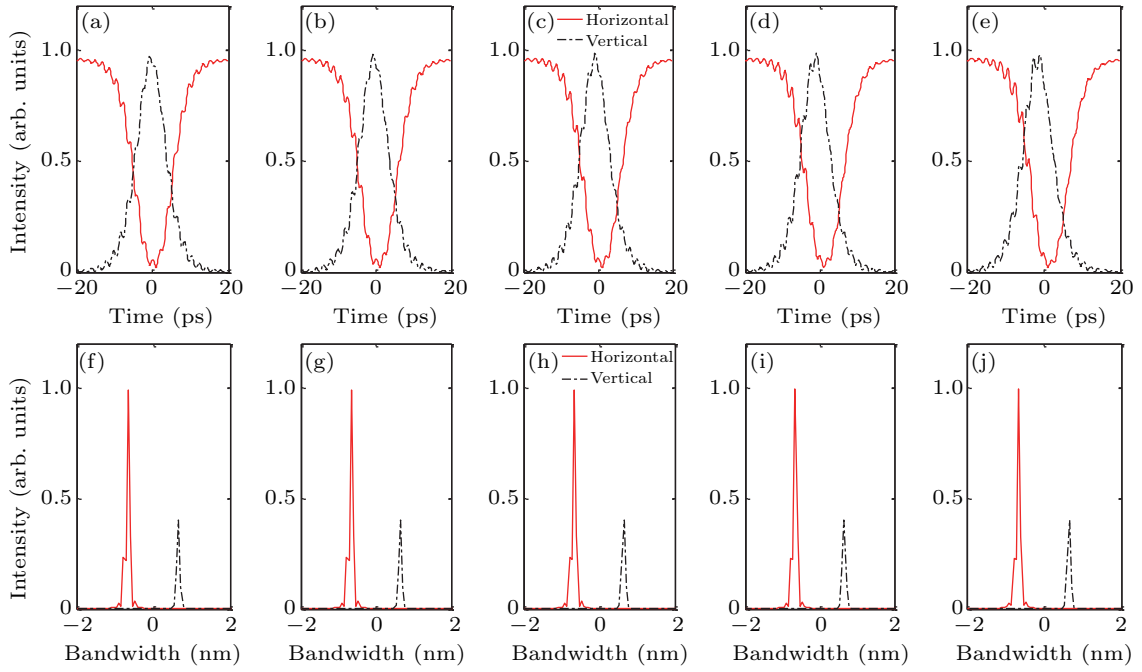


Fig. 14. Simulated pulses and optical spectra in orthogonal polarizations as ΔT and $\Delta\varphi$ change ($\lambda_1 \neq \lambda_2$).

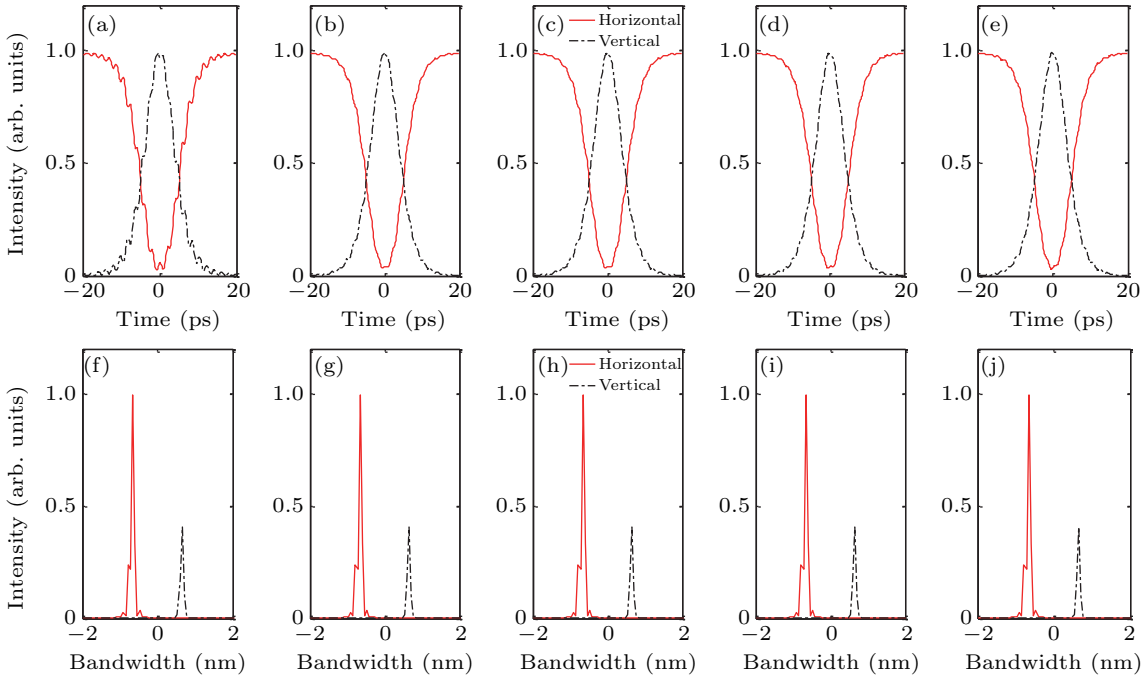


Fig. 15. Simulated pulses and optical spectra in orthogonal polarizations as θ and $\Delta\varphi$ change ($\lambda_1 \neq \lambda_2$).

Figure 14 gives the simulated pulses and optical spectra in horizontal and vertical polarizations ($\lambda_1 \neq \lambda_2$), when $\Delta T = 0.6$ ps, 1.2 ps, 1.8 ps, 2.4 ps and 3 ps. Meanwhile, $\Delta\varphi = \pi/10, \pi/9, \pi/8, \pi/7$ and $\pi/6$. $u_2/u_1 = 1/1$, $\theta = 3°$. As ΔT and $\Delta\varphi$ increase, both pulse shapes and corresponding optical spectra show no obvious changes, except for the increased time delay between the orthogonal pulses. This means that the variation of ΔT can only change the time delay between the orthogonal pulses under simultaneous changes in $\Delta\varphi$. Therefore, the bright-gray vector soliton with different orthogonal central wavelengths still maintains its robustness under variations in ΔT and $\Delta\varphi$.

Figure 15 gives the simulated pulses and optical spectra in horizontal and vertical polarizations ($\lambda_1 \neq \lambda_2$), when $\theta = 3°$, 6°, 9°, 12° and 15°. Meanwhile, $\Delta\varphi = \pi/10, \pi/9, \pi/8, \pi/7$ and $\pi/6$. $u_2/u_1 = 1/1$, $\Delta T = 0$ ps. In Figs. 15(a)–15(e), the orthogonal pulses have slight temporal oscillations when $\theta = 3°$ and $\Delta\varphi = \pi/10$. Then, the temporal curves become relatively smooth as both θ and $\Delta\varphi$ increase. This means that the increased $\Delta\varphi$ can efficiently compensate for the temporal oscillations (as indicated in Figs. 7(a)–7(e)) induced by θ. In Figs. 15(f)–15(j), the orthogonal optical spectra are robust to increasing values of θ and $\Delta\varphi$.

4. Discussion

In this work, the simulation results of manipulating a bright-gray vector soliton have specific application scenarios in the fields of long-distance polarization-multiplexed optical fiber communication, distributed optical fiber sensing, optical information processing, Bose–Einstein condensation, laser plasma, and so on.

Compared with traditional intra-cavity manipulation of optical solitons through the construction of fiber laser oscillators, the significance of our research is to split or combine the orthogonal components of the input vector soliton and manipulate them independently or together through variations in multiple parameters. This method can efficiently increase the tuning range and adjustment flexibility of the input vector soliton in the time or frequency domain. Besides, our physical model can also be expanded to manipulate other types of vector solitons.

5. Conclusion

We simulate the extra-cavity manipulation of a bright-gray vector soliton at a wavelength of 1 μm. Five kinds of parameters are changed to manipulate a bright-gray vector soliton, including central wavelengths (λ_1 and λ_2), amplitude ratio (u_2/u_1), projection angle (θ), time delay (ΔT), and phase difference ($\Delta\varphi$). The manipulated bright-gray vector soliton's orthogonal components demonstrate different evolution properties as different soliton parameters are varied. These simulation results effectively reveal the dynamics of a bright-gray vector soliton with the extra-cavity manipulation technique, further enriching the understanding of the nonlinear dynamic characteristics of bright-gray vector solitons.

Acknowledgments

Project supported by the National Natural Science Foundation of China (Grant Nos. 62105208 and 52172150) and

the College Students' Innovation and Entrepreneurship Training Program of Shanghai Institute of Technology (Grant Nos. S202610259346, X2026102590917, X2026102590923, and X2026102590927).

References

[1] Wang C Q, Zhao X Q, Zhang Y L and Lv Z W 2025 *Chin. Phys. B* **34** 124205
[2] Wang X M, Li J and Hu X X 2025 *Chin. Phys. B* **34** 110502
[3] Bao K Y, Tang X G and Wang Y 2024 *Chin. Phys. B* **33** 124203
[4] Rajan M S M, Triki H and Biswas A 2026 *Chaos Solitons Fractals* **202** 117539
[5] Yildirim Y, Biswas A and Asiri A 2024 *Nonlinear Dyn.* **112** 601
[6] Lan Z Z 2024 *Chin. Phys. B* **33** 060201
[7] Yi H H, Li X F, Zhang J L, Zhang X and Ma G L 2024 *Chin. Phys. Lett.* **41** 074204
[8] Li Y, Mu Y, Xi F, Wang X and Li X H 2025 *Opt. Laser Technol.* **183** 112304
[9] Zhang C H, Xiang P F, Zhu W, Chen C and Liu X M 2024 *Infrared Phys. Technol.* **142** 105572
[10] Lu J Y, Sun J X, Shu Y Q, Li J Q, Tiu Z C and Chen W C 2025 *Opt. Express* **33** 49150
[11] Shi Y R, Zhang H J, Ren Y X, Peng J S and Zeng H P 2025 *Chin. Phys. B* **34** 094207
[12] Zhuang L J, Feng H Y, Wang X P and Dai C Q 2025 *Chin. Phys. Lett.* **42** 120408
[13] Li K, Hu Q P, Chen W, Gao C, Feng H Y, Zhang Z R, Li X, Li Z F and Zhou Q 2025 *Chin. Phys. Lett.* **42** 120407
[14] Huang X W, Guo X X, Huang X Z, Peng F, Li X H, Wei Z Y and Wang Q J 2024 *Laser Photonics Rev.* **18** 202400166
[15] Li X H, Huang X Z, Han Y H, Chen E C, Guo P L, Zhang W M, An M Q, Pan Z W, Xu Q, Guo X X, Huang X W, Wang Y S and Zhao W 2023 *Ultrafast Sci.* **3** 0006
[16] Han Y H, Li X H, Chen E C, An M Q, Song Z Y, Huang X Z, Liu X F, Wang Y S and Zhao W 2022 *Adv. Opt. Mater.* **10** 2201034
[17] An M Q, Pan Z W, Li X H, Wang W, Jiang C, Li G, Guo P L, Lu H B, Han Y H, Chen X H and Zhang Z Y 2022 *ACS Appl. Mater. Interfaces* **14** 53971
[18] Ju Z T, Si Z Z, Yan X and Dai C Q 2024 *Chin. Phys. Lett.* **41** 084203
[19] Zhang B, Liu S S, Wang T J, Hou Y Z, Wang T S and Deng G 2026 *Opt. Commun.* **602** 132725
[20] Yu Y, Xu X T, Yao X K and Yang W L 2025 *Phys. Rev. A* **112** 063532
[21] Luo W B, Li Y, Nakkeeran K and Zhou R L 2025 *Phys. Rev. A* **112** 053522
[22] Du Y Q, Zhang Z Z, Zhang H Z, Xue J, Zeng C, Cui Y D, Mao D, Malomed B A and Zhao J L 2025 *Phys. Rev. Lett.* **135** 263801
[23] Zhang Z H, Duan X H, Zhang Y, Li Z Q, Zhang M B, Wang J L, Chen M J and Wei Z Y 2025 *Opt. Express* **33** 51549
[24] Xue J, Zhang Y F, Du Y Q, Zeng C, Li D, Cheng G H, Zhao J L and Mao D 2025 *Phys. Rev. A* **112** 033510
[25] Zhang J W, Yao Y, Guo L G, Qiu H X, Li S T, Ge C D, Lv Y Z, Tian J J, Xu X C and Duan J N 2026 *Opt. Laser Technol.* **200** 115152
[26] Guo J, Hu X, Song Y F, Shao G D, Zhao L M and Tang D Y 2019 *Phys. Rev. A* **99** 061802
[27] Yi H H, Yao Y L, Zhang X and Ma G L 2023 *Chin. Phys. B* **32** 100509
[28] Cui X N, Zhang Z Y, Liu M W, Qi F H and Liu W J 2025 *Chin. Phys. Lett.* **42** 100402
[29] Zhou H S, Zhang Z Y, Liu M W, Qi F H and Liu W J 2025 *Chin. Phys. Lett.* **42** 070001
[30] Wang L L and Liu W J 2020 *Chin. Phys. B* **29** 070502
[31] Zhou Y, Zhang K Y, Luo C, Lin X Y, Liao M S, Zhao G Y and Fang Y Z 2022 *Chin. Phys. B* **31** 054203
[32] Zhou Y, Li Y F, Fang Y Z and Liao M S 2020 *J. Technol.* **20** 196